Investigating Seasonality in Sulfate Presence and Radiative Forcing in the North Pacific

by

Jack Zweifel

A thesis submitted in partial fulfillment of

the requirements for the degree of

Master of Science in Atmospheric & Oceanic Sciences

at the

UNIVERSITY OF WISCONSIN-MADISON

2025

Date of Master's Thesis Presentation: 09/17/2025

The dissertation is approved by the following members of the Graduate Advising Committee:

Dan Vimont, Professor, Atmospheric and Oceanic Sciences
Dave Henderson, Assistant Professor, Atmospheric and Oceanic Sciences
Mayra Oyola-Merced, Assistant Professor, Atmospheric and Oceanic Sciences

Table of Contents

Abstract

Sulfate aerosols, formed from the atmospheric oxidation of sulfur dioxide (SO_2), are well-established contributors to global cooling through both direct and indirect radiative effects. Despite this, substantial uncertainties remain regarding their spatiotemporal distribution and resulting radiative effects, especially in relation to anthropogenic emissions and downstream burden. One underexplored aspect is the seasonal evolution of sulfate burden in response to changes in SO_2 emissions from East Asia. In this study, we employ the Community Earth System Model Version 2 (CESM2) to simulate the impact of varying East Asian anthropogenic SO_2 emissions on downwind sulfate aerosol burden over the North Pacific Ocean. Model experiments are run using unchanging meteorological conditions but with SO_2 emissions set at climatological levels from 1850, 1970, 2000, and 2006. While the SO_2 emissions themselves exhibit limited seasonality, North Pacific modeled sulfate burden shows a consistent seasonal cycle with minimums in boreal winter and peaks in late boreal spring. Through differencing experiments, we find that East Asian anthropogenic emissions account for up to 50% of the springtime sulfate burden in the downstream North Pacific. Enhanced springtime oxidation and chemical processing over East Asia largely explains the modeled sulfate seasonality. Further, we quantify the radiative effects of these aerosols, decomposing them into direct, indirect (cloud-mediated), and surface albedo components. All components contribute to regional cooling, with indirect radiative effects dominating the total radiative forcing. On average, indirect radiative forcing is an order of magnitude stronger than the direct effect and accounts for over 95% of the total aerosol-induced cooling in the North Pacific.

1. Introduction

Atmospheric aerosols are a key component of the climate system, influencing radiation, clouds, and precipitation through complex physical and chemical pathways (Forster et al., 2007; Liu et al., 2012). This study focuses on sulfate aerosols, which primarily form through the atmospheric oxidation of sulfur dioxide (SO_2) emitted from natural sources such as volcanic degassing, marine dimethyl sulfide, and from anthropogenic activities including coal combustion, biomass burning, and other industrial processes (Edmonds & Mather, 2017; Charlson et al., 1987; Benkovitz et al., 1996). Once emitted, SO_2 is oxidized via gas and aqueous-phase pathways to produce sulfate (referred to here as SO_4) aerosols (Barth et al., 2000; Chin et al., 1996). After their formation, sulfate aerosols have a lifetime of minutes to weeks in the troposphere (Szopa et al. 2021) leading to impacts downstream from their source regions. This study focuses on downwind impacts of anthropogenic East Asian tropospheric sulfate aerosols over the North Pacific Ocean.

Sulfate aerosols affect incoming solar radiation both directly through absorption and scattering and indirectly through their impact on clouds. Sulfate direct radiative effects largely stem from their ability to scatter incoming solar radiation, increasing planetary albedo and reducing the amount of shortwave energy reaching Earth's surface (Adams et al., 2001; Koch, 2001). As they are highly reflective and weak absorbers, sulfate aerosols act as strong shortwave cooling agents. In addition, sulfate indirect radiative effects arise from their role as cloud condensation nuclei (CCN) and their cloud mediating properties. By increasing the number of CCN, sulfate aerosols lead to the formation of smaller and more numerous cloud droplets which enhances cloud reflectivity, a phenomenon known as the cloud albedo effect (Twomey, 1977). In-cloud sulfate aerosols may also extend cloud lifetime by suppressing precipitation efficiency,

particularly in marine stratiform clouds, which further amplifies their cooling influence through what is referred to as the cloud lifetime effect (Albrecht, 1989). Together, these direct and indirect processes contribute to a significant net cooling, with sulfate aerosols estimated to exert a global mean radiative forcing of approximately –0.5 W m^{-2} relative to preindustrial conditions (Myhre et al., 2001).

To investigate these aerosol-climate interactions in a regional context, our study focuses on East Asia and the North Pacific Ocean (Fig 1). East Asia, defined here as China, Japan, and South Korea (red shading) is one of the world's dominant sources of anthropogenic SO_2 emissions and hence a large source for subsequent anthropogenic sulfate aerosol production. The prevailing westerly winds over the Northern Hemisphere suggest a large downwind effect over the North Pacific Ocean. The North Pacific (NPAC, blue hatched) region follows the "NPO" domain defined in the Intergovernmental Panel on Climate Change (IPCC) Sixth Assessment Report (Iturbide et al., 2020) with the southern boundary adjusted to 20°N to better capture East Asian SO_2 outflow.

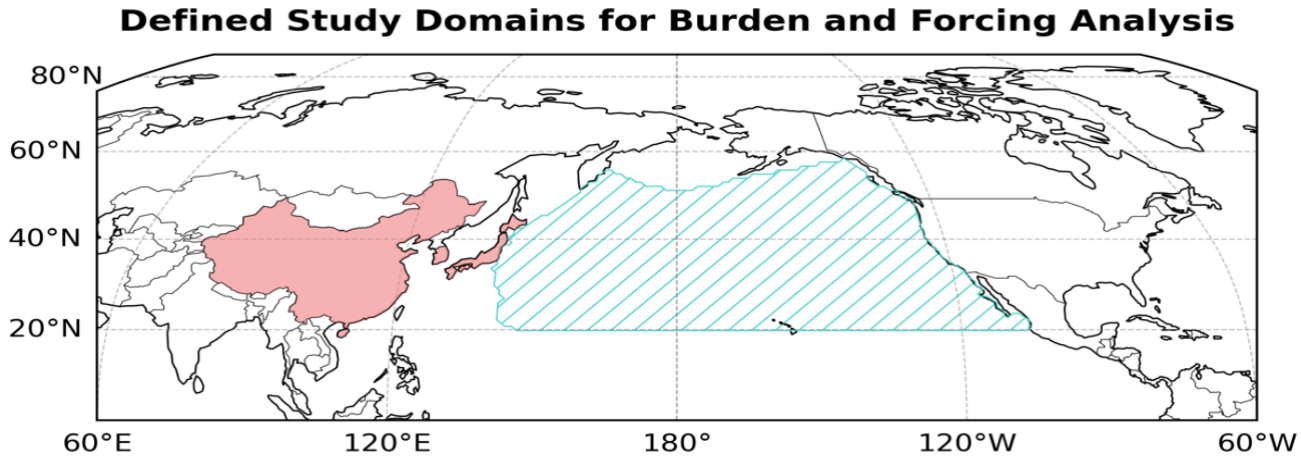

Figure 1 *Regional domains used in this study, including the East Asian source region (China, Japan, and South Korea) and the downwind North Pacific Ocean receptor region. This source-receptor framework provides the basis for analyzing the transport, transformation, and radiative impacts of sulfate aerosols originating from East Asian anthropogenic emissions.*

An apparent mismatch between the modeled seasonality of SO_2 emissions in East Asia and the seasonal cycle of sulfate burden over the downstream North Pacific motivates this study. Historical model simulations such as the Community Earth System Model's Large Ensemble-2 (Rodgers et al., 2021) show that although East Asian SO_2 emissions differ little across the year, simulated sulfate burden over the North Pacific exhibits a pronounced seasonal structure. Figure 2 illustrates this contrast, comparing the relatively unseasonal sulfur fluxes from East Asia with the growing spread of sulfate aerosol optical depth over the North Pacific. This disconnect suggests that processes beyond local emissions, such as atmospheric transport, chemical conversion rates, and meteorological variability play a critical role in shaping the observed seasonality. We note this same seasonality is seen in satellite estimates of sulfate aerosol optical depth over the North Pacific (Matus et al., 2019).

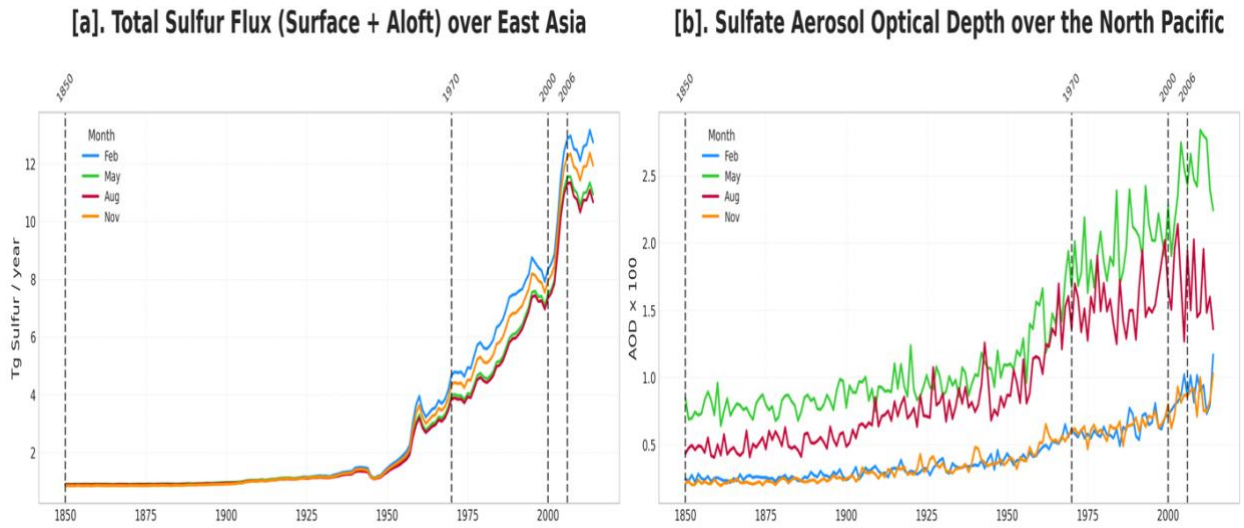

Figure 2 *Seasonal evolution of East Asian SO_2 emissions and downwind sulfate aerosol optical depth (AOD) over the North Pacific from a single member of the CESM2 large ensemble simulations. [a] Total sulfur emissions from China, Japan, and South Korea show little seasonal variation. [b] In contrast sulfate AOD exhibits an offset, pronounced, and growing seasonal cycle with springtime maxima. Vertical dashed lines mark benchmark years (1850, 1970, 2000, 2006) referenced later in model experiments.*

Recent work by Rathod et al. (2025) examined a similar seasonal relationship over the North Atlantic, focusing on how reductions in U.S. SO_2 emissions between 1970 and 2010 affected downstream sulfate burden seasonality and radiative forcing. Despite minimal seasonality in U.S. SO_2 emissions, Rathod et al. showed pronounced seasonal differences in sulfate burden, with summertime values up to three-to-five times higher than winter values. Reductions in U.S. SO_2 emissions weakened this seasonality by roughly 20%, primarily due to decreased summertime chemical production and transport of sulfate. These changes also produced a disproportionately large summertime radiative forcing (~2 W m^{-2}) compared to winter (~0.9 W m^{-2}), highlighting the strong seasonal sensitivity of sulfate aerosols and climate interactions to regional emission changes.

In this study, we mirror the work of Rathod et al. (2025) but focus on the evolution of East Asian SO_2 emissions and the resulting downwind sulfate burdens over the North Pacific Ocean. This is accomplished using an earth system model run with custom emissions datasets in which East Asian SO_2 emissions are varied while background meteorology and all other global aerosol sources are held constant. This modeling framework allows us to isolate and investigate the role of regional emissions and atmospheric processes in driving the seasonal evolution of sulfate burden and associated radiative forcing over the North Pacific. Throughout this work we investigate the East Asia-North Pacific system through four guiding questions:

1. What are the spatial and temporal characteristics of seasonal sulfate aerosol burden over the North Pacific, and how do they evolve with increasing East Asian anthropogenic emissions?
2. What processes drive the large seasonal cycle of sulfate burden over the North Pacific?

3. How and why did this seasonality strengthen from 1970 to 2006 as East Asian industrial emissions increased?
4. What are the resulting seasonal impacts on top-of-atmosphere radiative forcing across this period?

The paper is organized as follows: Section 2 describes the model framework, radiative metrics, and experimental design used to isolate East Asian sulfate forcing. Section 3 presents results and discussion, including the seasonal evolution and spatial distribution of modeled sulfate burden, a budget-based attribution of seasonality, and the temporal and spatial characteristics of radiative forcing components. Section 4 summarizes the key findings and broader implications for aerosol-climate interactions. Lastly Section 5 details current and future work involved in this research.

2. Materials and Methods

2.1 Overview

This study investigates how variations in historical East Asian sulfur dioxide (SO_2) emissions have shaped the seasonal evolution of sulfate (SO_4) aerosols and their radiative influence over the downwind North Pacific. We focus on sulfate burden as a key diagnostic linking emission-driven changes in atmospheric sulfate concentrations to perturbations in shortwave radiative fluxes via both direct scattering and indirect cloud-mediating effects. Following the methodological framework of Rathod et al. (2025), we isolate the impact of East Asian SO_2 emissions by holding global meteorology and non-East Asian emissions fixed while varying sulfurous emissions over East Asia. The model configuration and full experimental design are described below.

2.2 Model Description

Model: We run the Community Earth System Model version 2.1.5 (CESM2.1.5) which utilizes the Community Atmosphere Model version 6 (CAM6; Hurrell et al., 2013; Liu et al., 2012). The model resolution is approximately 0.93° latitude by 1.25° longitude, featuring 56 vertical hybrid-sigma pressure levels ranging from the surface (~1000 hPa) to the model top (~2 hPa). Our specific model uses the standard F2000 configuration, which approximates modern conditions using an average 1995–2005 climatology (Rasch et al., 2019). While later periods benefit from substantially improved global aerosol observing systems, F2000 remains the default CESM baseline for fixed-oxidant, climatological simulations. To isolate the effect of chemistry and aerosol physics, model simulations are run using “nudged” meteorology, in which the atmospheric state is relaxed to prescribed conditions. Meteorological conditions are prescribed using Modern-Era Retrospective analysis for Research and Applications version 2 (MERRA-2;

Rienecker et al., 2011) reanalysis data from 2000 onward, employing the default 50-hour relaxation timescale.

Chemistry: While CESM includes a detailed sulfur chemistry scheme (Liu et al., 2012), we adopt a simplified configuration that captures the dominant pathways of sulfate formation. In this setup the model tracks sulfate aerosols as both interstitial particles that are independently suspended in the atmosphere and cloud-borne aerosols that are activated within droplets. Modeled sulfates are formed through gas-phase oxidation with hydroxyl radicals (OH) and aqueous-phase reactions involving hydrogen peroxide (H_2O_2) and ozone (O_3) (Tie et al., 2001). The CESM simple chemistry prescribes these key oxidants and aligns well with existing chemistry and the Community Earth System Model's Large Ensemble-2 (Danabasoglu et al., 2020).

Aerosol: CESM employs the four-mode Modal Aerosol Module for resolving aerosol microphysics (MAM4; Liu et al., 2016). Processes modeled include new particle formation, condensation, coagulation, and aqueous uptake. Removal processes such as dry deposition, gravitational settling, and wet scavenging (both in-cloud and below-cloud) are also explicitly treated, allowing the model to realistically evolve aerosol mass and size distributions over time (Liu, 2023).

CESM's representation of sulfate aerosols has been extensively evaluated in previous studies, which collectively demonstrate strong agreement with modeled and observed sulfate concentrations (Ge et al., 2022, Tilmes et al., 2023). Rathod et al. (2025) compared modeled surface sulfate from CESM against ground-based observations from the EPA Chemical Speciation Network and IMPROVE datasets, finding close alignment in both magnitude and

seasonality. While sparse observations over East Asia and the North Pacific limit direct evaluation, these prior validations support confidence in CESM2's ability to capture the processes governing sulfate aerosol variability in our study region.

2.3 Model Experiments

The anthropogenic aerosol and precursor emissions used in this study are sourced from the Community Emissions Data System (CEDS; Hoesly et al., 2018). Figure 3 presents the historical evolution of SO_2 emissions from CEDS in East Asia and highlights the four benchmark years that serve as prescribed emissions scenarios for our model simulations. This includes: 1850 (pre-industrial baseline), 1970 (rapid industrial growth), 2000 (modern control climatology), and 2006 (peak emissions). These benchmark years are indicated by vertical dashed lines. All three countries show distinct growth periods, with China contributing the largest absolute increase in emissions. Across all nations, energy production, industrial combustion, and residential consumption dominate the emissions profile, consistent with prior assessments (Hoesly et al., 2018).

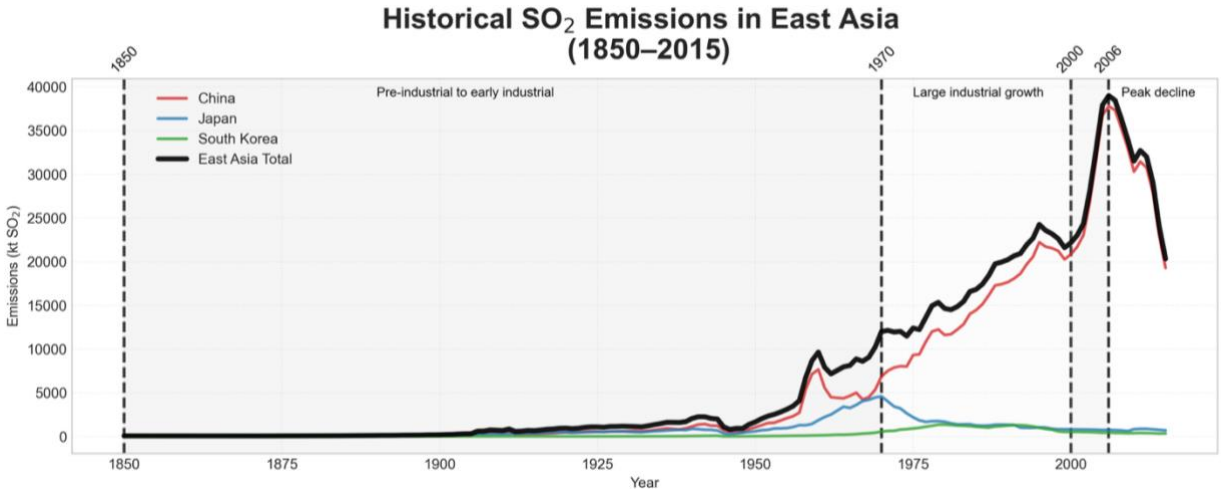

Figure 3. *Historical SO_2 emissions from China, Japan, and South Korea from the Community Emissions Data System (CEDS) for 1850–2015 detailing the total annual SO_2 emissions by country. Vertical dashed lines mark the four benchmark years (1850, 1970, 2000, 2006) used as East Asian emission scenarios in CESM2 simulations.*

From the selected years in Figure 3 (vertically dashed lines) we design four model experiments in CESM2 corresponding to these benchmark years, hereafter referred to as E.A. 1850, E.A. 1970, E.A. 2000, and E.A. 2006. In each experiment, East Asian SO_2 and direct sulfate emissions are prescribed according to the selected benchmark year, while global emissions from all other regions are fixed to the year-2000 climatology (1995-2005 average). Table 1 organizes our modeling approach and is presented below.

Table 1. *Summary of CESM2 experiments used to isolate the radiative forcing of East Asian SO_2 and sulfate aerosol emissions. Each simulation prescribes East Asian emissions for a benchmark year while keeping all other regions fixed to the year-2000 climatology. Pairwise comparisons between these experiments are used to quantify historical changes in sulfate forcing.*

Simulation Name	Benchmark Year	East Asian SO_2 / SO_4 Emissions Level	Purpose
E.A. 1850	1850	Pre-industrial baseline	Provides low-emission reference for estimating historical radiative forcing.
E.A. 1970	1970	Industrial growth period	Used as "base" year for forcing calculations and comparison to U.S. sulfate studies.
E.A. 2000	2000	Modern control climatology	Represents control simulation for present-day climate.
E.A. 2006	2006	Peak East Asian emissions	Represents maximum East Asian sulfate forcing scenario.

Each simulation is integrated for 10.5 years, with the initial six months discarded as spin-up following Rathod et al. (2020). This integration length is sufficient to capture interannual variability while allowing the model to reach equilibrium in aerosol and radiative fields. To isolate the climatic response to East Asian SO_2 emissions, subsequent analyses rely primarily on pairwise differencing between differing simulations. In particular, the E.A. 2006 and E.A. 1970 simulations that represent the transition from a period of rapid industrial growth to peak regional emissions. These two experiments serve as anchor points for evaluating changes in sulfate burden, transport, and radiative effects discussed in Section 3.

2.4 Sulfate Aerosol Radiative Effects

Radiative interactions with aerosols in CAM6 are computed using the Rapid Radiative Transfer Model for General Circulation Models (RRTMG; Iacono et al., 2008). Using RRTMG, we distinguish between radiative effects, which refer to the instantaneous impact of sulfate aerosols on net shortwave fluxes under fixed atmospheric conditions, and radiative forcing which captures how that influence changes across different emissions scenarios. We apply the diagnostic method from Ghan (2013) and Ghan et al., (2012) in which paired radiative transfer calls are used to isolate both the aerosol direct and indirect impacts. To do this, RRTMG is called in parallel across multiple distinct atmospheric configurations within the same model timestep (for diagnostic purposes only), each representing a different combination of clouds and sulfate aerosols as seen in Table 2 and illustrated in Figure 4

Table 2. *Atmospheric configurations used in the paired-call RRTMG diagnostic for isolating sulfate aerosol radiative effects. When compared across differing emission simulations, these effects are used to calculate changes in anthropogenic direct, cloud, and surface albedo radiative forcing components. (see text for formulas)*

Configuration Name	Clouds Included?	Sulfate Aerosols Included?	Other Aerosols Included?	Symbol in Equations
Total-sky	Yes	Yes	Yes	F
Clean-sky	Yes	No	Yes	F_{clean}
Clear-sky	No	Yes	Yes	F_{clear}
Clean-clear-sky	No	No	Yes	$F_{clean,clear}$

Each forcing component is computed as the change in radiative effects between a high-emission and a low-emission simulation, corresponding here to the E.A. 2006 and E.A. 1970 experiments. In this framework, Δ denotes the difference between time periods (2006 – 1970), and each *F* represents a net shortwave flux at the top of the atmosphere within one of the four atmospheric configurations. For example, direct radiative forcing is calculated as:

$$DRF \;=\; \Delta(F - F_{clean}) = (F - F_{clean})_{2006} - (F - F_{clean})_{1970}$$

Note that under the "Clean-sky" scenario below, cloud properties such as cloud droplet radius (which influences cloud albedo) are unchanged from the "Total-sky" scenario, ensuring that indirect effects can be calculated from the differences below. Analogous expressions are used for the indirect radiative forcing and surface albedo forcing components. These configurations allow us to compute different components of the net shortwave radiative forcing at the top of the atmosphere. By comparing the radiative fluxes from the multiple RRTMG calls in the 2006 and 1970 emissions simulations, we identify three key radiative forcing metrics:

1. Direct Radiative Forcing $\Delta(F - F_{clean})$: quantifies the total direct absorption and scattering radiative impacts a change in sulfate aerosol amount.
2. Indirect Radiative Forcing $\Delta\left(F_{clean} - F_{clean,clear}\right)$: captures sulfate induced modifications to cloud radiative properties between two simulations.
3. Surface Albedo Forcing Δ $(F_{clean,clear})$: reflects sulfate-driven changes in surface reflectivity between two simulations.

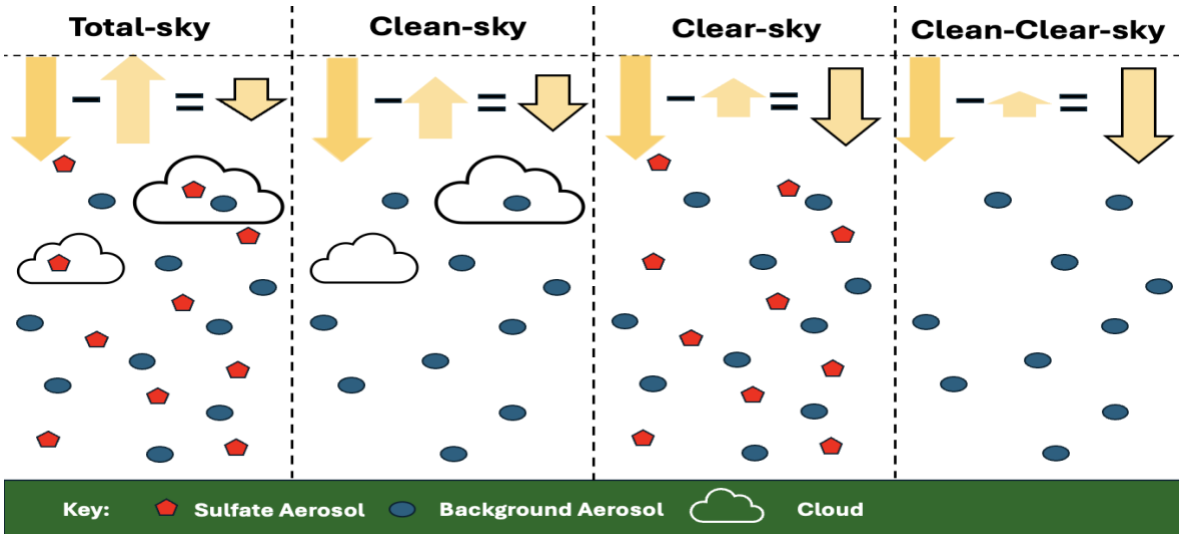

Figure 4. *Illustrated atmospheric configurations used in the paired-call RRTMG diagnostic for isolating sulfate aerosol radiative effects. Arrows represent downward, upward, and net shortwave radiative fluxes at the top of atmosphere. When compared across differing emission simulations, these effects are used to calculate changes in anthropogenic direct, cloud, and surface albedo radiative forcing components.*

3. Results and Discussion

3.1 Sulfate Burden Seasonality & Spatial Distribution

Figure 5a shows the monthly climatology of modeled sulfate burden over NPAC across our four simulations. All simulations display a pronounced seasonal cycle, with burdens peaking during April-June (AMJ) and reaching a minimum during November-January (NDJ). This modeled seasonality aligns with prior findings where Yang et al. (2019) attribute weaker modeled wintertime sulfate formation to reduced photochemical activity, aircraft observations from Van Donkelaar et al. (2008) detail enhanced springtime sulfate concentrations downwind of East Asia, and Matus et al. (2019) document comparable seasonality in satellite-retrieved aerosol optical depth over the North Pacific. In addition to the baseline seasonality, Figure 5a shows that the spring-winter contrast strengthens steadily with rising emissions. While sulfate burden increases in both seasons, the total is greater in spring, leading to a progressively larger seasonal amplitude from 1850 to 2006.

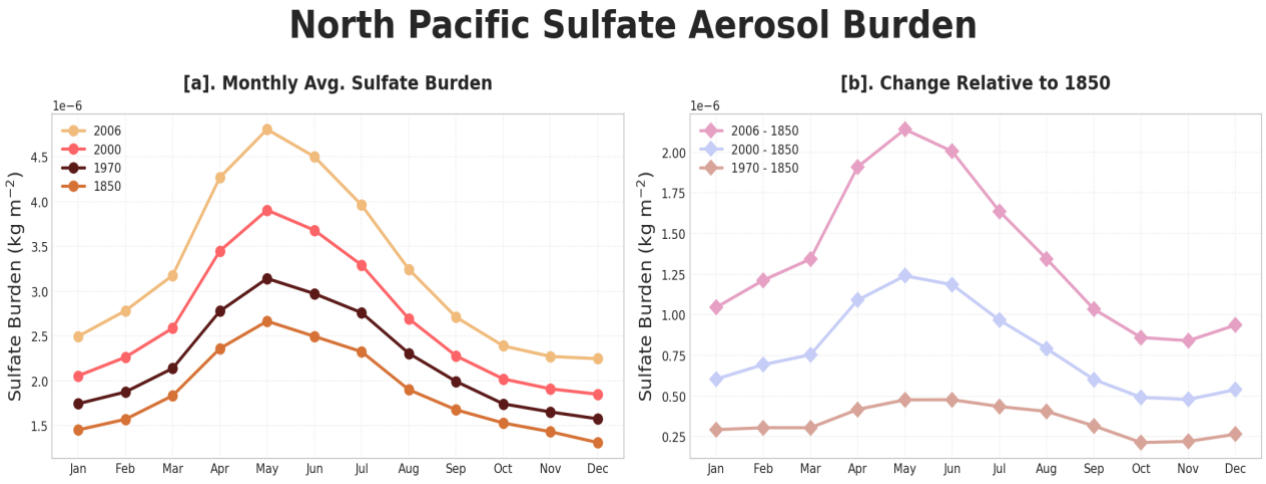

Figure 5. *Monthly climatologies of sulfate aerosol burden over the North Pacific from CESM2 simulations with varying East Asian SO_2 emissions (1850, 1970, 2000, 2006). [a] Total burden shows a strong seasonal cycle with peaks in April-June and minima in November-January. [b] Differences relative to 1850 isolate the incremental contribution of East Asian emissions.*

Figure 5b highlights the change in sulfate burden relative to the preindustrial E.A. 1850 simulation which contains only background and natural sources. Because all simulations share the same non-East Asian emissions fixed at year-2000 levels, this differencing approach effectively cancels out external contributions and isolates the incremental sulfate burden attributable to varying stages of East Asian industrialization. All three simulation differences share a consistent seasonal pattern as values rise through late winter, peak in AMJ, and decline through summer and autumn, reaching a minimum in early winter. This pattern largely mirrors the total climatology from each simulation in Figure 5a but with amplitudes that grow steadily across industrial periods as the 1970 experiment peaks near 0.5×10^{-6} kg m^{-2}, while the 2000 and 2006 cases reach roughly 1.25×10^{-6} and over 2.0×10^{-6} kg m^{-2} respectively. To contextualize the 2006 East Asian contribution to the North Pacific sulfate burden, we compare three related measures:

a. The isolated NPAC sulfate burden from 2006 East Asian emissions (top curve in fig 5b),

b. The total NPAC sulfate burden from the full 2006 emissions simulation (top curve in fig 5a), and

c. The background burden present in the absence of East Asian emissions (bottom curve in fig 5a)

Comparing these three measures provides us with two complementary perspectives on isolated burdens from 2006 East Asian anthropogenic emissions - one that is relative to the total 2006 atmosphere and one relative to the year 2000 background. When viewed as a fraction of the total 2006 burden (**a/b**), East Asian anthropogenic emissions account for roughly 41% of the sulfate present over the North Pacific. When compared against the baseline background (**a/c**), the

same increment represents about 71% of the sulfate burden: this represents the increase in sulfate aerosol burden in 2006 relative to what would have been there if there were no East Asian emissions. The contribution is also seasonally dependent, with the largest fractional increases in spring and weaker enhancements in winter, reinforcing the springtime sensitivity identified earlier. To assess where these contrasts are spatially concentrated, we next examine the distributions of sulfate burden during AMJ and NDJ.

Figure 6 illustrates the spatial distribution of sulfate burden for the AMJ, when burdens reach their seasonal maximum, and NDJ, when they reach their minimum, along with the difference between the two. The top row shows total sulfate burden from the E.A. 2006 simulation (analogous to Fig 5a), while the bottom row shows the corresponding differences between the E.A. 2006 and E.A. 1970 simulations (analogous to Fig 5b), isolating the contribution from increased East Asian emissions.

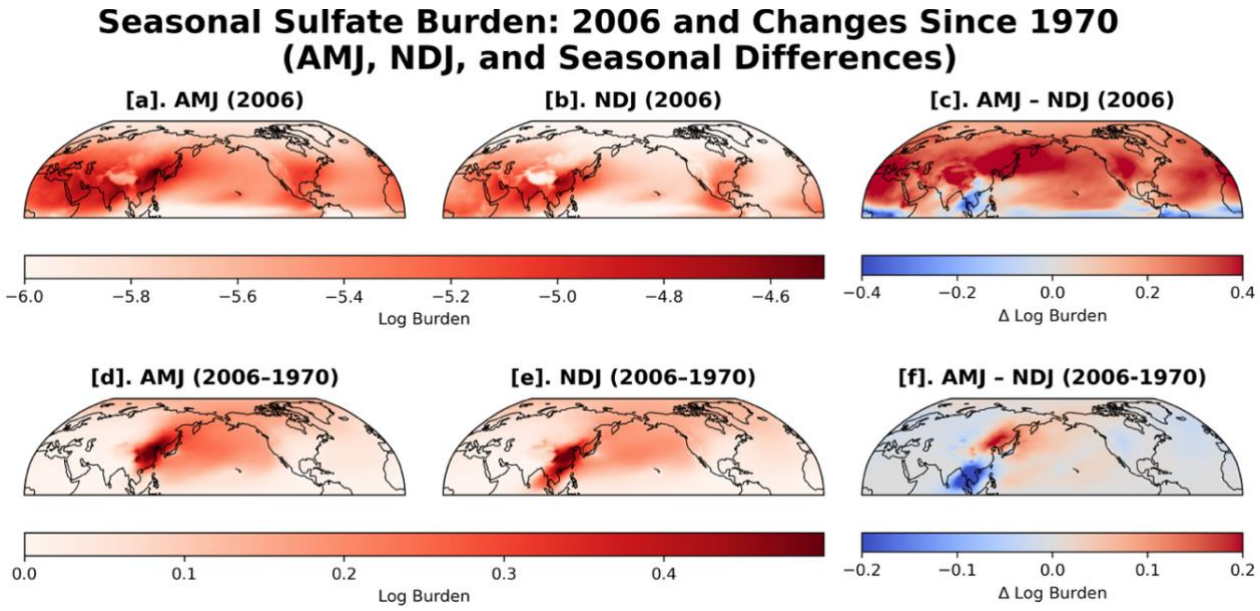

Figure 6. *Spatial distributions of sulfate burden over the North Pacific Ocean during the AMJ (peak) and NDJ (minimum) seasons, and their seasonal difference (peak minus minimum). Sulfate burdens are shown as log values and calculated from the E.A, 2006 and E.A. 2006 – E.A. 1970 simulation differences, representing the downwind sulfate enhancement attributable to East Asian industrial emissions.*

In the top row of Fig. 6, the E.A. 2006 simulation reflects both East Asian and background (year-2000) global sources. Elevated sulfate burden is apparent across the Northern Hemisphere midlatitudes, with particularly high values over East Asia and the North Pacific during AMJ compared to NDJ. The AMJ – NDJ panel highlights this seasonal contrast, with enhanced sulfate extending across the midlatitude Pacific and diminished concentrations during winter.

In the bottom row of Fig. 6, the differenced simulations remove the background contribution, revealing the spatial fingerprint of East Asian industrialization. Enhanced sulfate is evident across northern China and the downstream North Pacific during AMJ consistent with the seasonality established in figure 5, while NDJ shows weaker and more localized enhancement centered farther south. The difference panel reinforces this pattern, with positive anomalies spanning northern China to the central Pacific with a smaller negative lobe over Southeast Asia illustrating the spatial seasonal drift in NPAC burden. Collectively, figures 5 and 6 highlight both the spatial and temporal seasonal differences in sulfate burden over the North Pacific stemming from East Asian anthropogenic emissions

3.2 Attribution of Changing Sulfate Seasonality

Tables 3 and 4 summarize the seasonal SO_2 and SO_4 budget differences between the E.A. 2006 and E.A. 1970 simulations for the East Asian source region and the downwind NPAC receptor region. All quantities represent the net change between the high- and low-emission scenarios, expressed in units of kg S for burden and kg S sec^{-1} for emission, production, deposition, and transport. Seasonal values were computed by averaging AMJ and NDJ monthly means and summing across each respective region.

Table 3 & 4. *SO_2 and SO_4 budgets computed from simulation differences E.A. 2006 – E.A. 1970 in which sulfurous East Asian anthropogenic emissions were varied while outside global emissions were kept at a year 2000 climatological levels. All quantities represent the net change between the high- and low-emission scenarios, expressed in units of kg S for burden and kg S sec^{-1} for emission, production, deposition, and transport.*

	2006-1970			
SO_2 Budget:	**East Asia**		**North Pacific**	
	AMJ	**NDJ**	**AMJ**	**NDJ**
(a) SO_2 Burden	4.40×10^7	7.61×10^7	5.12×10^6	4.40×10^6
(b) SO_2 Emission	428.8	463.5	0	0
(c) $SO_2 \rightarrow$ SO4 aq. Chem.	45.6	33.7	9.6	14.2
(d) $SO_2 \rightarrow$ SO4 dry Chem.	88.9	42.1	6.4	2.0
(e) SO_2 Dry Deposition	131.3	180.8	0.9	0.2
(f) SO_2 Wet Deposition	103.1	91.2	0.3	0.3
(g) SO_2 Transport	59.9	115.7	-17.3	-16.8

	2006-1970			
SO_4 Budget:	**East Asia**		**North Pacific**	
	AMJ	**NDJ**	**AMJ**	**NDJ**
(a) SO_4 Burden	2.37×10^7	1.45×10^7	1.28×10^7	5.46×10^6
(b) SO_4 Emission	11.0	11.9	0	0
(c) $SO_2 \rightarrow$ SO4 aq. Chem.	45.6	33.7	9.6	14.2
(d) $SO_2 \rightarrow$ SO4 dry Chem.	88.9	42.1	6.4	2.0
(e) SO_4 Dry Deposition	15.6	15.5	2.9	2.0
(f) SO_4 Wet Deposition	89.3	44.0	26.4	23.3
(g) SO_4 Transport	40.5	28.2	-13.2	-9.0

Over East Asia, SO_2 burden is much larger in NDJ than AMJ (AMJ/NDJ ≈ 0.58), reflecting slightly stronger winter emissions and suppressed oxidation during the cold season. In contrast, SO_4 burden peaks in AMJ (AMJ/NDJ ≈ 1.64). Downstream over the NPAC, SO_2 burden shows only weak seasonality (AMJ/NDJ ≈ 1.16), while SO_4 burden more than doubles

from NDJ to AMJ (AMJ/NDJ ≈ 2.35), demonstrating that the Pacific experiences greatest sulfate loading in spring despite East Asia having its largest SO_2 burden in winter.

Emissions differ only over East Asia, where combined SO_2 and SO_4 emissions are slightly smaller in AMJ than NDJ (AMJ/NDJ ≈ 0.93) following the seasonal emission patterns seen in Figure 2. No emission differences occur over NPAC as no emissions were varied in the region, confirming that all downwind changes arise from transport and chemistry rather than evolving local sources. Compared to emissions, sulfate chemical production exhibits much stronger seasonality, especially over East Asia. In East Asia, aqueous production of SO_4 is higher in AMJ (AMJ/NDJ ≈ 1.36), and gas-phase (dry) production is more than twice as large in AMJ (AMJ/NDJ ≈ 2.11), yielding a total SO_2-to-SO_4 chemical conversion rate about 1.8 times higher in spring than winter. Over the NPAC, total SO_4 chemical production remains nearly constant between seasons, but the dominant oxidation pathways shift as AMJ features a relatively balanced split between aqueous and dry production, whereas NDJ production is dominated by aqueous processes. This reflects the strong springtime increase in OH and the wintertime reliance on ozone-driven aqueous oxidation (Fig. 7).

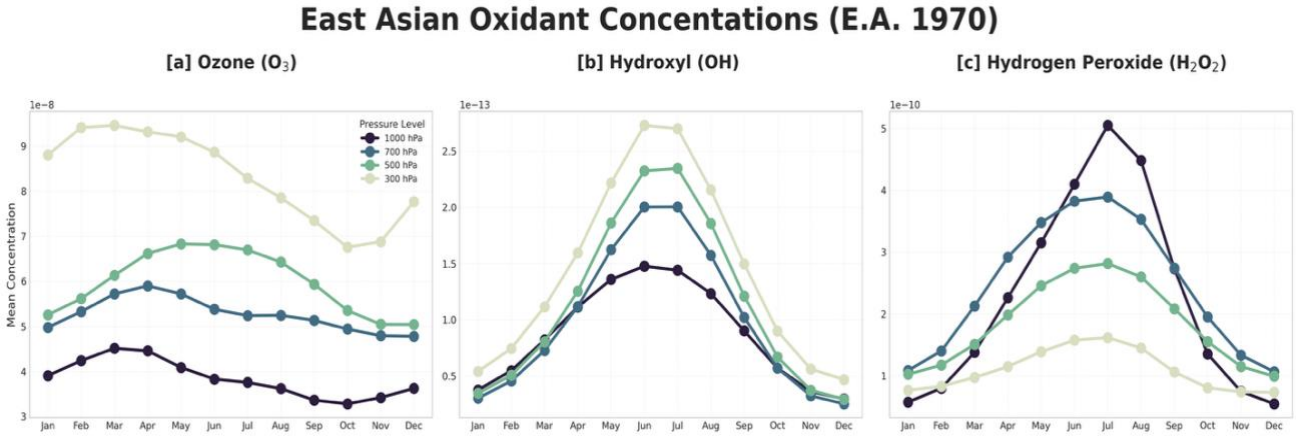

Figure 7. *Monthly climatologies of sulfate oxidant concentrations over the East Asia from simulation E.A. 1970. [a] O_3 concentration peaks in winter and increases with height. [b] OH concentrations have a strong peak in summer and increase with height. [c] H_2O_2 concentrations also peak in summer but decrease with height.*

Deposition patterns further reinforce these contrasts. Over East Asia, SO_2 dry deposition is larger in NDJ (AMJ/NDJ ≈ 0.73), consistent with the higher SO_2 burden, while SO_4 dry deposition varies little between seasons. Wet deposition of SO_4, however, is much larger in AMJ (AMJ/NDJ ≈ 2.03), mirroring the strong seasonal peak in sulfate burden. Over NPAC, deposition fluxes are far smaller in magnitude but show similar tendencies as SO_4 dry and wet deposition: both wet and dry deposition are slightly larger in AMJ, consistent with higher springtime sulfate loading.

Transport terms represent the net divergence of sulfur from a region and complete the sulfur budget. These terms are calculated from residuals as they are not directly output by the model. Positive values indicate net exports of species from a region and negative values indicate a net import. The SO_2 budget terms summarized in Table 3 show that emissions are the sole source (term b) while losses include chemical conversion and total deposition (c + d + e + f). This yields substantial export from East Asia, about 60 kg S sec^{-1} in AMJ and 116 kg S sec^{-1} in NDJ, and a nearly constant net convergence of about 17 kg S sec^{-1} into the NPAC region. The SO_4 budget in Table 4 similarly indicates that sources consist of direct emissions and chemical production (b + c + d), while sinks include dry and wet deposition (e + f). East Asia exports approximately 41 kg S sec^{-1} of SO_4 in AMJ and 28 kg S sec^{-1} in NDJ, of which approximately 13 kg S sec^{-1} in AMJ and 9 kg S sec^{-1} in NDJ converge over the NPAC (the remaining flux out of East Asia is deposited elsewhere).

Taken together, the sulfate budget reveals a clear seasonal narrative linking East Asian emissions to downwind sulfate presence over the North Pacific. Winter features high SO_2 burden over East Asia driven by elevated emissions and weak oxidation, but relatively little of this SO_2

is converted to sulfate before export. In spring, by contrast, enhanced oxidant availability over East Asia substantially increases gas-phase and aqueous chemical conversion of SO_2 to SO_4, boosting regional sulfate burden despite slightly lower emissions. The net result is that SO_4 burden increases and SO_2 burden decreases over East Asia in spring, and the region correspondingly exports more sulfate and less SO_2 at that time. Over the North Pacific, SO_2 import is relatively constant between winter and spring, as is the subsequent production of SO_4 due to offsetting seasonality of gas-phase and aqueous production. The enhanced import of SO_4 from East Asia during spring thus represents an enhanced source of SO_4 during spring.

This springtime shift in chemical production leads to greater SO_4 export from East Asia and weaker SO_2 export, and it produces a correspondingly stronger influx of sulfate into the North Pacific even though SO_2 export itself reaches its maximum in winter. Together, these results show that the springtime sulfate maximum over the North Pacific is driven not by the magnitude of SO_2 emissions alone, but by the seasonally enhanced efficiency of SO_2-to-SO_4 conversion and the subsequent transport of sulfate-rich air masses.

3.3 Radiative Forcing

We now shift from sulfate burden to its radiative impacts, using the paired-call RRTMG diagnostic described in Section 2.4 to quantify how sulfate aerosols alter the top-of-atmosphere (TOA) shortwave flux. Following the decomposition in Ghan et al. (2012), we isolate the indirect, direct, and surface albedo components of radiative forcing by differencing TOA radiative effects between the E.A. 2006 and E.A. 1970 simulations over the NPAC basin.

Negative values indicate cooling associated with increased anthropogenic sulfate (Figure 8).

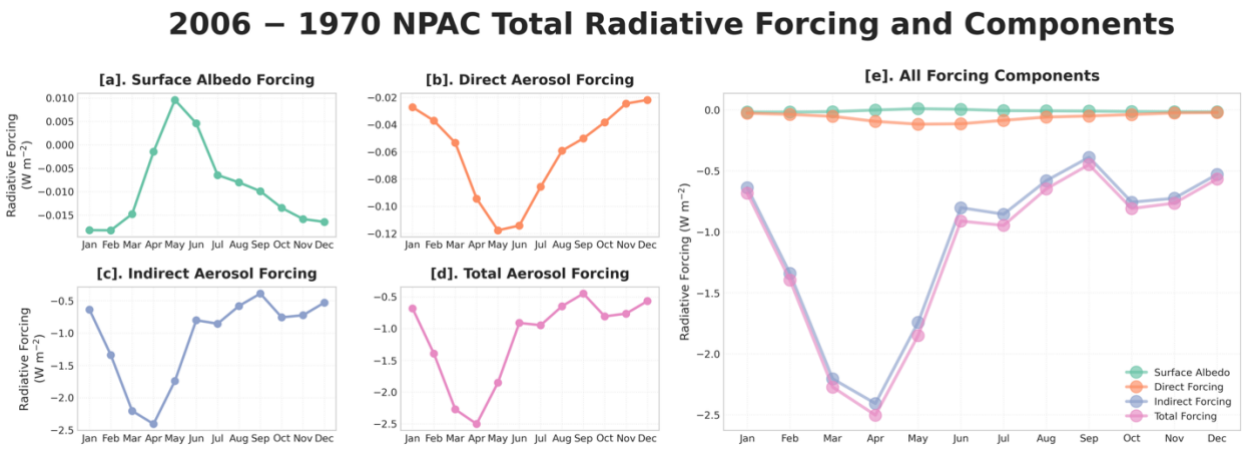

Figure 8. *Monthly climatologies of sulfate aerosol radiative forcing over the North Pacific, computed as the difference between E.A. 2006 and E.A. 1970 simulations. Panels show [a] surface albedo forcing, [b] direct aerosol forcing, [c] indirect aerosol forcing, [d] total forcing as the sum of all three components, and (f) all components plotted together.*

3.3.1 Timing of Radiative Forcing Components

a. Indirect Radiative Forcing

Across Figure 8 we see that the indirect (cloud mediated) radiative forcing, shown in panel [c], dominates the total sulfate forcing (which is calculated as the sum of all the individual components). Peak indirect forcing values exceed –2 W m^{-2} in March and April and account for roughly 95% of the total cooling when averaged across the year. The seasonal maximum in radiative cooling occurs in April with an average forcing of –2.4 W m^{-2}. This maximum in cooling also occurs one month earlier than the peak in NPAC sulfate burden and direct forcing as seen in Figure 5 and Figure 6. Compared to the climatologies of NPAC sulfate burden and direct forcing, the indirect radiative forcing also has comparatively greater month to month variability as secondary fluctuations with local minimums also occur in July, and from October through November. Although the magnitude and timing of this indirect forcing strongly suggest underlying adjustments in cloud microphysics and cloud amount, the present analysis does not explicitly evaluate the cloud response. Fully attributing the indirect effect would require

additional diagnostics such as changes in cloud droplet number concentration, liquid water path, cloud fraction, or vertically resolved sulfate activation pathways, which lie beyond the scope of this study but represent an important direction for future work.

b. Direct Radiative Forcing

The direct radiative forcing contributes a smaller but steady cooling throughout the year, with magnitudes ranging from about –0.03 W m^{-2} in winter to –0.11 W m^{-2} in May. This seasonal maximum coincides with the North Pacific sulfate burden peak (Figure 5), indicating that the direct scattering response scales closely with the aerosol loading pattern. Compared to the indirect forcing, the direct component exhibits a much smoother seasonal evolution, decreasing gradually from January to early summer and then recovering toward its initial winter values. The close temporal alignment between sulfate burden and direct forcing reflects their common physical basis, whereas the earlier spring maximum in cloud forcing suggests that cloud adjustments begin while the atmosphere is still transitioning toward its highest sulfate concentrations.

c. Surface Albedo Forcing

Lastly, the surface albedo component remains weak (± 0.01 W m^{-2}) and spatially incoherent across the region (not shown). Its negligible contribution reflects the limited interaction of sulfate surface reflectivity changes to low-albedo ocean surfaces.

d. Total Radiative Forcing

When combined, the three components yield a total sulfate radiative forcing that mirrors the indirect radiative forcing component, with peak cooling exceeding –2.5 W m^{-2} in April and a minimum near –0.5 W m^{-2} in boreal winter. The right panel of Figure 8 shows all the individual

components and the total plotted together on the same axes and highlights the additive nature of the forcers. The dominance of the indirect component ensures that the total forcing retains both its amplitude and its seasonality, while the direct contribution acts to slightly strengthen the overall signal. To better understand where these seasonal contrasts manifest geographically, we next examine the spatial distributions of direct and indirect forcing across the North Pacific basin.

3.3.2 Spatial Extent

Figure 9 presents the spatial distributions of indirect and direct radiative forcing between the E.A. 2006 and E.A. 1970 simulations. These are the same forcing components shown previously in the climatological time series, but with retained spatial structure. The first two columns illustrate the radiative forcing components during AMJ and NDJ, the peak and minimum seasons of NPAC sulfate burden while the third column shows their seasonal differences (AMJ – NDJ), highlighting the contrast between the high and low seasons.

a. Indirect Forcing Extent

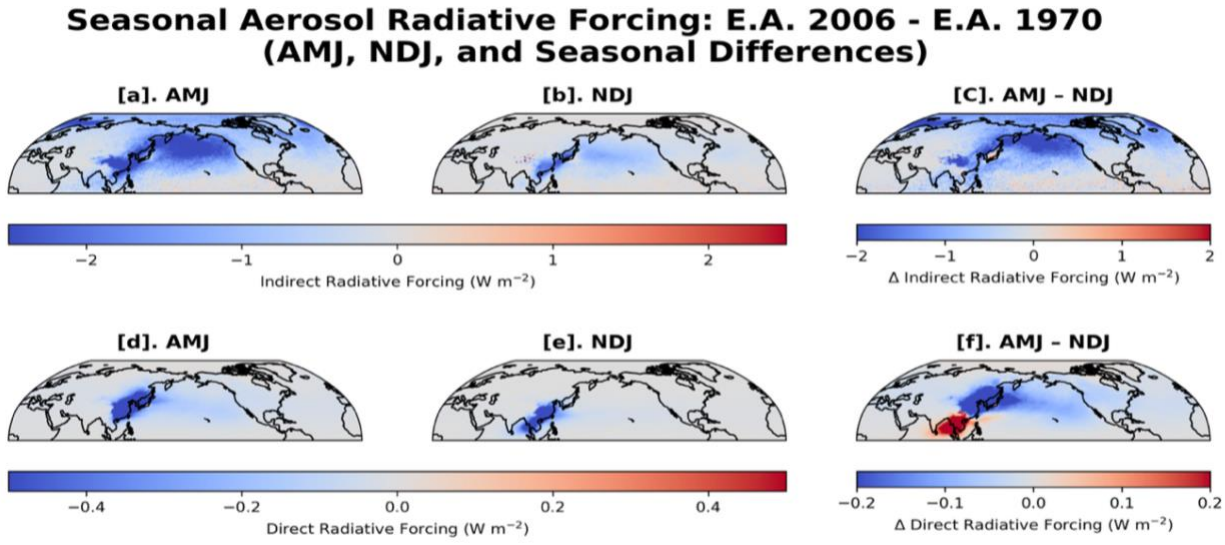

Figure 9. *Seasonal spatial climatologies and differences of indirect and direct sulfate aerosol radiative forcing over the North Pacific, computed as the difference between E.A. 2006 and E.A. 1970 simulation. Top row illustrates the seasonal variance of indirect radiative forcing and bottom row illustrates the variance of direct radiative forcing.*

In the top row of Figure 9, the indirect radiative forcing exhibits a broad spatial extent and far greater magnitude and footprint than its direct counterpart. During AMJ, cooling extends across nearly the entire North Pacific basin, averaging –1.7 W m^{-2} and reaches local minima stronger than –3 W m^{-2}. The strongest responses occur over the downstream Pacific and into the midlatitudes, consistent with widespread cloud enhancement along the primary outflow pathways from East Asia. Elevated cooling also appears more broadly across the Northern Hemisphere, though the dominant signal remains concentrated over the North Pacific.

In NDJ, both the magnitude and spatial extent of the cooling weaken, with basin-mean values of –0.6 W m^{-2}. Cooling becomes confined mainly to the North Pacific and coastal East Asia, reflecting the reduced cloud mediated cooling during winter. This reduction is consistent with the seasonal cloud climatology and lower insolation during NDJ, which limit the shortwave radiative impact of aerosol-induced cloud modifications even when sulfate perturbations are present. The seasonal difference map emphasizes that springtime enhancements in sulfate burden produce basin-wide increases in cloud forcing, contrasting with the more spatially confined and mixed direct forcing response. The coherence and magnitude of this pattern further emphasize that aerosol-cloud interactions dominate the regional shortwave cooling signature.

b. Direct Forcing Extent

The bottom row of Figure 9 details the localized fingerprint of the direct radiative forcing. Just as the climatological timeseries of direct radiative forcing aligns well with the timeseries of NPAC sulfate burden, a clear relationship can be seen between the spatial distributions of direct forcing and sulfate burden. The direct radiative forcing closely follows the differences in sulfate structure between simulations shown in the bottom row of Figure 6.

During AMJ, cooling averages around –0.1 W m^{-2} across the basin, with maxima near -0.4 W m^{-2} over the ocean and localized values exceeding –2 W m^{-2} over land. The influence extends eastward across the North Pacific occasionally reaching the west coast of North America. In NDJ, the magnitude and coverage of the cooling weaken substantially, with mean values measuring –0.02 W m^{-2} and a contraction of the forcing field toward Southeast Asia. The seasonal difference map reveals a dipole-like structure of enhanced cooling over northern East Asia and the North Pacific with a weaker, more localized winter pattern centered over Southeast Asia. This pattern closely mirrors the AMJ – NDJ difference in sulfate burden shown in Figure 6. The strong physical linkage between aerosol burden and direct radiative forcing is evident as seasonally higher (lower) sulfate concentrations produce seasonal stronger (weaker) burden dependent shortwave cooling.

3.3.3 Context with other Forcers

To place these results in context, peak sulfate indirect radiative forcing in our simulations exceeds –2 W m^{-2} in some regions, locally comparable in magnitude to the global mean radiative forcing from well-mixed greenhouse gases since preindustrial times. The IPCC AR6 estimates that the total forcing from long-lived greenhouse gases over 1750–2011 is +2.91 W m^{-2}, with CO_2 contributing +2.16 W m^{-2}, CH_4 contributing +0.54 W m^{-2}, and N_2O contributing +0.16 W m^{-2} (IPCC AR6 Chapter 7). Unlike these globally distributed, persistent, and positive forcings, sulfate impacts are negative, highly regional, and strongly seasonal. This juxtaposition highlights the disproportionate role that regional aerosol-cloud interactions can play in shaping Earth's energy balance despite their more localized and transient nature compared to greenhouse gases.

3.4 Caveats

Assumptions that could affect the quantitative interpretations are summarized here. First, atmospheric oxidant concentrations (OH, H_2O_2, O_3) are prescribed from year-2000 conditions across all simulations. While this ensures a consistent chemical environment between simulations, these oxidant concentrations may not represent 1850, 1970, and 2006 conditions. As a result, sulfate production may be slightly overestimated or underestimated relative to true historical atmospheres. In addition, the year-2000 baseline does not correspond to the period of strongest observational constraint on global aerosol and oxidant fields. Many of the most capable satellite observing systems, including CALIPSO, CloudSat, OMI, and later MODIS/MISR collections, did not become available until after 2004-2006. These instruments significantly improved global aerosol detection and the quality of assimilation products such as MERRA-2. Thus, while F2000 remains the standard CESM climatological background for controlled perturbation experiments, it does not necessarily reflect the best-characterized modern aerosol environment.

Second, natural and anthropogenic aerosol backgrounds (e.g., dust, sea salt, black carbon) are also fixed at year-2000 levels. Aerosol microphysical processes such as condensation, coagulation, and wet deposition depend on background aerosol concentrations so maintaining a modern background may introduce nonlinearities, particularly in low-emissions scenarios.

Third, sulfate aerosols are dynamically partitioned between interstitial and cloud-borne modes in CESM2. Processes such as evaporation, cloud cycling, and wet scavenging interact to determine the evolving sulfate mass. Although these processes are explicitly represented in the

model, diagnosing the full contributions of cloud processing and scavenging pathways to sulfate burden would require more detailed microphysical analysis beyond the scope of this study.

4. Summary

We perform a suite of CESM2.1.5 simulations in which only East Asian SO_2 and directly emitted sulfate are varied to represent 1850, 1970, 2000, and 2006 conditions, in order to investigate how regional industrialization shapes the spatial, seasonal, and radiative characteristics of sulfate aerosols over the North Pacific Ocean (NPAC). Although East Asian SO_2 emissions themselves exhibit little seasonal variability, they produce a pronounced and strengthening seasonal cycle in downwind NPAC sulfate burden as emissions increase. Sulfate burdens peak during spring (April-May-June) and reach minima during winter (November-December-January) producing basin wide increases with higher emissions amplifying both the mean burden and the seasonal contrast.

Sulfur budget diagnostics demonstrate that this seasonality arises from seasonal differences in chemical processing and transport efficiency rather than emissions alone. Tables 3 and 4 show that springtime conditions favor rapid aqueous- and gas-phase oxidation of SO_2, enabling efficient sulfate formation near the source and enhanced export into the free troposphere, where sulfate is more readily transported across the North Pacific. In contrast, wintertime conditions limit oxidant availability and suppress chemical conversion, reducing sulfate production and long-range transport despite comparable emissions. As a result, increases in East Asian emissions disproportionately enhance springtime sulfate export and accumulation over the NPAC, strengthening the seasonal cycle.

This enhanced sulfate burden produces a strongly seasonal radiative response. Between the 1970 and 2006 simulations, the combined direct and cloud-mediated top-of-atmosphere radiative forcing becomes increasingly negative, with basin-mean cooling of approximately –1.8

W m^{-2} in spring (MAM) compared to roughly –0.7 W m^{-2} in winter (NDJ). The radiative response is dominated by the indirect cloud-mediated component and peaks during the season of maximum sulfate production and export, highlighting the sensitivity of NPAC radiative forcing to the timing of emissions relative to atmospheric chemical and dynamical conditions.

These results advance the current understanding of aerosol-climate interactions by demonstrating that the climatic impact of anthropogenic sulfate emissions depends not only on emission magnitude, but on how emissions project onto seasonally varying chemical, transport, and cloud regimes. While sulfate aerosol forcing is often discussed in terms of annual or global-mean effects, this study shows that regional aerosol-cloud interactions can exhibit strong, emission-driven seasonality that substantially modulates radiative forcing on seasonal timescales. By explicitly linking evolving anthropogenic emissions to changes in seasonal sulfate processing, export efficiency, and cloud-mediated radiative forcing, this work provides a mechanistic framework for interpreting regional aerosol forcing and its role in shaping North Pacific climate variability.

5. Current and Future Work

Building on the results presented in Section 3.3.1, ongoing work is aimed at decomposing the indirect (cloud-mediated) radiative forcing into its underlying physical components, including Twomey-type microphysical pathways and Albrecht-type cloud-amount adjustments. As part of this effort, I have begun exploring differences in cloud droplet number concentration, liquid water path, and cloud fraction between the 1970 and 2006 simulations to better understand which cloud regimes contribute most strongly to the basin-wide cooling response. These analyses are still preliminary and not yet suitable for publication, but they represent an important step toward linking the diagnosed indirect radiative forcing to explicit cloud and aerosol microphysical changes.

A continuing component of this project, conducted with Dan Vimont and Sagar Rathod, explores whether aerosol radiative effects and radiative forcing can be computed without explicitly calling RRTMG, the shortwave radiative transfer model used within CESM. Because RRTMG is computationally expensive, especially in paired-call mode that must be run separately for every timestep, developing a reduced-cost surrogate has the potential to dramatically accelerate future modeling work. This includes developing radiative kernels based on a set of 60 CESM ensemble simulations in which global SO_2 emissions were systematically perturbed from 0.1 times to 6 times their baseline values. For each ensemble member, RRTMG was used to compute direct and indirect sulfate radiative effects, producing a smooth, structured dataset that can be used to estimate sensitivities of radiative fluxes to aerosol and cloud properties.

In parallel with this kernel-based approach, I developed a machine learning framework to emulate RRTMG directly using standard model output. The premise is that if the relationship between the atmospheric state and the radiative response is sufficiently regular, then a trained neural network could reproduce RRTMG results at a small fraction of the computational cost. I began by assembling the 60-member ensemble into a consolidated dataset containing monthly output on a 192 × 288 grid with 32 vertical levels and over 500 modeled variables. For initial development we focused on the North Atlantic Ocean, which substantially reduced the spatial extent while preserving relevant aerosol–cloud–radiation interactions. After this regional restriction, the training dataset consisted of 938,160 individual samples, each representing a unique combination of ensemble member, month, latitude, and longitude.

Feature construction relied on domain knowledge, previous research (Pal et al., 2019), and salient feature extraction techniques. Nineteen variables known or suspected to influence sulfate radiative effects were selected with vertically resolved variables contributing a feature for each level, resulting in a final input space of 237 standardized predictors as seen in table 5.

Table 5. *Feature matrix the Neural Network is trained and evaluated upon where each feature is extracted from the 60-member ensemble simulations.*

Variable	Long Name	Vertical Levels	Units
Cosine Month	Cyclic Monthly Time Encoding	1	1
Sine Month	Cyclic Monthly Time Encoding	1	1
PMID	Pressure at Layer Midpoint	32	Pa
T	Temperature	32	K
O3_vmr	Ozone Volume Mixing Ratio	32	mol/mol
OH_vmr	Hydroxyl Volume Mixing Ratio	32	mol/mol
H2O2	Hydrogen Peroxide Concentration	32	mol/mol
CLOUD	Cloud Fraction	32	Fraction
SOLIN	Solar Insolation	1	W/m2
ALDIF	Albedo: Longwave, Diffuse	1	1
ALDIR	Albedo: Longwave, Direct	1	1
ASDIF	Albedo: Shortwave, Diffuse	1	1
ASDIR	Albedo: Shortwave, Direct	1	1
AODABS	Aerosol Absorption Optical Depth 550 nm, Day Only	1	1
AODUV	Aerosol Optical Depth 350 nm, Day Only	1	1
AODVIS	Aerosol Optical Depth 550 nm, Day Only	1	1
AODNIR	Aerosol Optical Depth 1020 nm, Day Only	1	1
SSAVIS	Aerosol Single-Scatter Albedo, Day Only	1	1
CDNUMC	Vertically-Integrated Droplet Concentration	1	1/m2
CLDLIQ	Grid Box Averaged Cloud Liquid Amount (Mixing Ratio: Wet)	32	Kg/Kg
Cumulative Array Size	237		

Standardization was necessary because these variables span a wide range of units and magnitudes; without rescaling, the neural network would disproportionately weight large-magnitude features and learn unstable gradients. After standardization, a fully connected feed-forward neural network was constructed with two hidden layers and ReLU activations. The network jointly predicted the direct and indirect radiative effects as computed by RRTMG. Training used mean squared error loss and the Adam optimizer with an 80/20 train–test split and 50 epochs, and performance was evaluated using the coefficient of determination (R^2) after inverse-transforming outputs back into physical units.

Because early experiments showed that the model's performance was highly sensitive to hyperparameters such as learning rate and neuron count, I used Ray Tune to perform randomized hyperparameter searches. The spread in outcomes was substantial: depending on the choice of hyperparameters, explained variance ranged from below 20% to above 95%. The best model used 128 neurons per hidden layer and a learning rate of approximately 0.005, achieving 95.6% explained variance for the direct effect and 97.2% for the indirect effect across all ensembles,

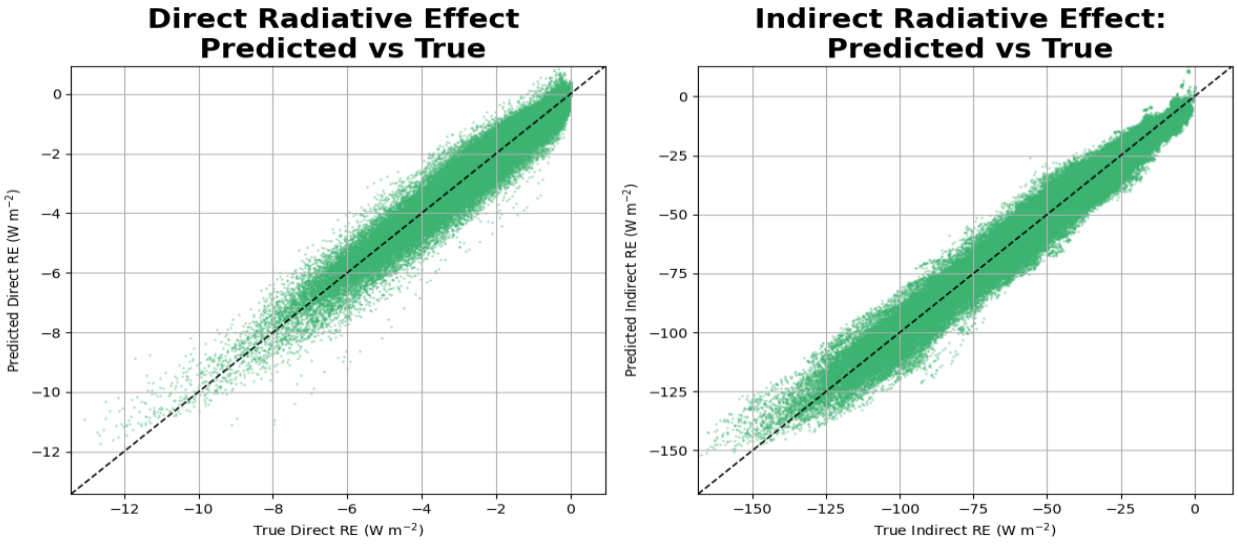

Fig 10. *Scatterplots comparing the neural-network–predicted direct (left) and indirect (right) sulfate radiative effects to the corresponding values computed by RRTMG for all ensemble members, months, and grid points within the North Atlantic domain. The dashed 1:1 line indicates perfect agreement. Points cluster tightly around this line for both components.*

months, and spatial points in the North Atlantic domain. The performance of the neural network emulator is illustrated in Figures 10 and 11. Figure 10 shows predicted versus true radiative effects for both the direct and indirect components. The points lie tightly along the 1:1 line, indicating that the network captures both the magnitude and spatial–temporal variability of the RRTMG output. This agreement holds across the full dynamic range, including the strongest cooling responses in the indirect effect.

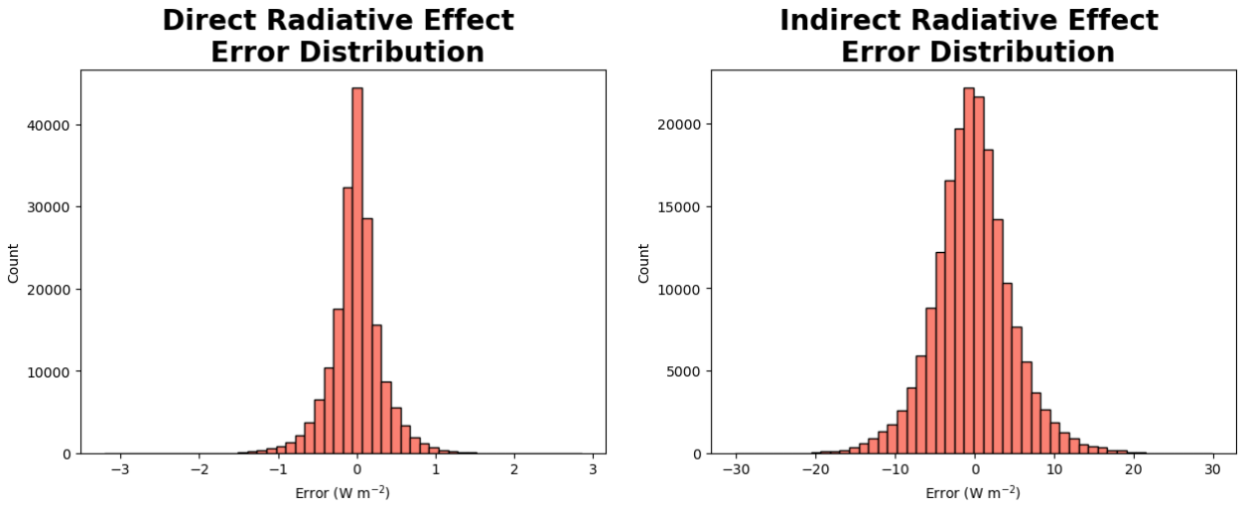

Fig 11. *Histograms of neural-network prediction errors for the direct (left) and indirect (right) sulfate radiative effects. Both distributions are centered near zero, indicating minimal systematic bias. Errors for the direct effect are concentrated within roughly ±1 W m^{-2}, while errors for the indirect effect fall largely within ±10 W m^{-2} despite its substantially larger physical range.*

Figure 11 shows the corresponding error distributions. Both distributions are centered extremely close to zero, with narrow spreads relative to the magnitude of the underlying signals. The direct-effect errors are concentrated within about ±1 W m^{-2}, while indirect-effect errors largely fall within ±10 W m^{-2} despite the much broader range of indirect radiative effects. These diagnostics demonstrate that the emulator is not only accurate in a global R^2 sense but also unbiased and well-behaved across regimes.

Together, these results show that machine learning can emulate RRTMG with surprisingly high fidelity when provided with sufficient ensemble diversity and physically meaningful features. This opens several promising directions for future work. One natural next step is to expand training beyond the North Atlantic to other basins and eventually to the global domain, which will test the generality of the learned relationships. Another direction is to experiment with architectures that incorporate physical structure more explicitly, such as convolutional layers that exploit vertical coherence or attention mechanisms that allow the model to weight physically important predictors. Embedding physical constraints, such as monotonicity or energy-conservation conditions, may further enhance interpretability and robustness. A key test will be integrating the emulator into CESM workflows to evaluate its performance during online simulations and to quantify potential computational speedups. Finally, comparing this neural-network approach with the radiative-kernel framework will help clarify the trade-offs between nonlinear flexibility and analytic interpretability, and may point toward hybrid methods that combine the strengths of both.

REFERENCES

Adams, P. J., Seinfeld, J. H., Koch, D., Mickley, L., & Jacob, D. (2001). General circulation model assessment of direct radiative forcing by the sulfate-nitrate-ammonium-water inorganic aerosol system. *Journal of Geophysical Research: Atmospheres*, *106*(D1), 1097–1111. https://doi.org/10.1029/2000JD900512

Albrecht, B. A. (1989). Aerosols, Cloud Microphysics, and Fractional Cloudiness. *Science*, *245*(4923), 1227–1230. https://doi.org/10.1126/science.245.4923.1227

Barth, M. C., Rasch, P. J., Kiehl, J. T., Benkovitz, C. M., & Schwartz, S. E. (2000). Sulfur chemistry in the National Center for Atmospheric Research Community Climate Model: Description, evaluation, features, and sensitivity to aqueous chemistry. *Journal of Geophysical Research: Atmospheres*, *105*(D1), 1387–1415. https://doi.org/10.1029/1999JD900773

Benkovitz, C. M., Scholtz, M. T., Pacyna, J., Tarrasón, L., Dignon, J., Voldner, E. C., et al. (1996). Global gridded inventories of anthropogenic emissions of sulfur and nitrogen. *Journal of Geophysical Research: Atmospheres*, *101*(D22), 29239–29253. https://doi.org/10.1029/96JD00126

Charlson, R. J., Lovelock, J. E., Andreae, M. O., & Warren, S. G. (1987). Oceanic phytoplankton, atmospheric sulphur, cloud albedo and climate. *Nature*, *326*(6114), 655–661. https://doi.org/10.1038/326655a0

Chin, M., Jacob, D. J., Gardner, G. M., Foreman-Fowler, M. S., Spiro, P. A., & Savoie, D. L. (1996). A global three-dimensional model of tropospheric sulfate. *Journal of Geophysical Research: Atmospheres*, *101*(D13), 18667–18690. https://doi.org/10.1029/96JD01221

Danabasoglu, G., Lamarque, J. -F., Bacmeister, J., Bailey, D. A., DuVivier, A. K., Edwards, J., et al. (2020). The Community Earth System Model Version 2 (CESM2). *Journal of Advances in Modeling Earth Systems*, *12*(2), e2019MS001916. https://doi.org/10.1029/2019MS001916

Edmonds, M., & Mather, T. A. (2017). Volcanic Sulfides and Outgassing. *Elements*, *13*(2), 105–110. https://doi.org/10.2113/gselements.13.2.105

Forster, P., Ramaswamy, V., Artaxo, P., Berntsen, T., Betts, R., Fahey, D. W., et al. (2007). Changes in Atmospheric Constituents and in Radiative Forcing. In *Climate Change 2007: The Physical Science Basis*. Cambridge, United Kingdom and New York, NY, USA: Cambridge University Press. Retrieved from https://www.ipcc.ch/site/assets/uploads/2018/02/ar4-wg1-chapter2-1.pdf

Ge, W., Liu, J., Xiang, S., Zhou, Y., Zhou, J., Hu, X., et al. (2022). Improvement and Uncertainties of Global Simulation of Sulfate Concentration and Radiative Forcing in CESM2. *Journal of Geophysical Research: Atmospheres*, *127*(20), e2022JD037623. https://doi.org/10.1029/2022JD037623

Ghan, S. J. (2013). Technical Note: Estimating aerosol effects on cloud radiative forcing. *Atmospheric Chemistry and Physics*, *13*(19), 9971–9974. https://doi.org/10.5194/acp-13-9971-2013

Ghan, S. J., Liu, X., Easter, R. C., Zaveri, R., Rasch, P. J., Yoon, J.-H., & Eaton, B. (2012). Toward a Minimal Representation of Aerosols in Climate Models: Comparative Decomposition of Aerosol Direct, Semidirect, and Indirect Radiative Forcing. *Journal of Climate*, *25*(19), 6461–6476. https://doi.org/10.1175/JCLI-D-11-00650.1

Hoesly, R. M., Smith, S. J., Feng, L., Klimont, Z., Janssens-Maenhout, G., Pitkanen, T., et al. (2018). Historical (1750–2014) anthropogenic emissions of reactive gases and aerosols from the Community Emissions Data System (CEDS). *Geoscientific Model Development*, *11*(1), 369–408. https://doi.org/10.5194/gmd-11-369-2018

Hurrell, J. W., Holland, M. M., Gent, P. R., Ghan, S., Kay, J. E., Kushner, P. J., et al. (2013). The Community Earth System Model: A Framework for Collaborative Research. *Bulletin of the American Meteorological Society*, *94*(9), 1339–1360. https://doi.org/10.1175/BAMS-D-12-00121.1

Iacono, M. J., Delamere, J. S., Mlawer, E. J., Shephard, M. W., Clough, S. A., & Collins, W. D. (2008). Radiative forcing by long-lived greenhouse gases: Calculations with the AER radiative transfer models. *Journal of Geophysical Research: Atmospheres*, *113*(D13), 2008JD009944. https://doi.org/10.1029/2008JD009944

Intergovernmental Panel On Climate Change (Ipcc). (2023). *Climate Change 2021 – The Physical Science Basis: Working Group I Contribution to the Sixth Assessment Report of the Intergovernmental Panel on Climate Change* (1st ed.). Cambridge University Press. https://doi.org/10.1017/9781009157896

Iturbide, M., Gutiérrez, J. M., Alves, L. M., Bedia, J., Cerezo-Mota, R., Cimadevilla, E., et al. (2020). An update of IPCC climate reference regions for subcontinental analysis of climate model data: definition and aggregated datasets. *Earth System Science Data*, *12*(4), 2959–2970. https://doi.org/10.5194/essd-12-2959-2020

Koch, D. (2001). Transport and direct radiative forcing of carbonaceous and sulfate aerosols in the GISS GCM. *Journal of Geophysical Research: Atmospheres*, *106*(D17), 20311–20332. https://doi.org/10.1029/2001JD900038

Kramer, R. J., Matus, A. V., Soden, B. J., & L'Ecuyer, T. S. (2019). Observation-Based Radiative Kernels From CloudSat/CALIPSO. *Journal of Geophysical Research: Atmospheres*, *124*(10), 5431–5444. https://doi.org/10.1029/2018JD029021

Liu, X., Easter, R. C., Ghan, S. J., Zaveri, R., Rasch, P., Shi, X., et al. (2012). Toward a minimal representation of aerosols in climate models: description and evaluation in the Community Atmosphere Model CAM5. *Geoscientific Model Development*, *5*(3), 709–739. https://doi.org/10.5194/gmd-5-709-2012

Liu, X., Ma, P.-L., Wang, H., Tilmes, S., Singh, B., Easter, R. C., et al. (2016). Description and evaluation of a new four-mode version of the Modal Aerosol Module (MAM4) within version 5.3 of the Community Atmosphere Model. *Geoscientific Model Development*, *9*(2), 505–522. https://doi.org/10.5194/gmd-9-505-2016

Liu, Xiaohong. (2023). Aerosols and Climate Effects. In Y. Liu & P. Kollias (Eds.), *Geophysical Monograph Series* (1st ed., pp. 53–86). Wiley. https://doi.org/10.1002/9781119529019.ch3

Matus, A. V., L'Ecuyer, T. S., & Henderson, D. S. (2019). New Estimates of Aerosol Direct Radiative Effects and Forcing From A-Train Satellite Observations. *Geophysical Research Letters*, *46*(14), 8338–8346. https://doi.org/10.1029/2019GL083656

Myhre, G., Myhre, A., & Stordal, F. (2001). Historical evolution of radiative forcing of climate. *Atmospheric Environment*, *35*(13), 2361–2373. https://doi.org/10.1016/S1352-2310(00)00531-8

Pal, A., Mahajan, S., & Norman, M. R. (2019). Using Deep Neural Networks as Cost-Effective Surrogate Models for Super-Parameterized E3SM Radiative Transfer. *Geophysical Research Letters*, *46*(11), 6069–6079. https://doi.org/10.1029/2018GL081646

Rathod, S., Vimont, D. J., Zweifel, J., Mahajan, S., Tilmes, S., Liu, X., et al. (2025). Impact of US SO_2 Emission Reductions Between 1970 and 2010 on Seasonal Sulfate Aerosol Burden and Radiative Forcing Over the North Atlantic. *Geophysical Research Letters*, *52*(20), e2025GL115337. https://doi.org/10.1029/2025GL115337

Rathod, S. D., Hamilton, D. S., Mahowald, N. M., Klimont, Z., Corbett, J. J., & Bond, T. C. (2020). A Mineralogy-Based Anthropogenic Combustion-Iron Emission Inventory. *Journal of Geophysical Research: Atmospheres*, *125*(17), e2019JD032114. https://doi.org/10.1029/2019JD032114

Rienecker, M. M., Suarez, M. J., Gelaro, R., Todling, R., Bacmeister, J., Liu, E., et al. (2011). MERRA: NASA's Modern-Era Retrospective Analysis for Research and Applications. *Journal of Climate*, *24*(14), 3624–3648. https://doi.org/10.1175/JCLI-D-11-00015.1

Rodgers, K. B., Lee, S.-S., Rosenbloom, N., Timmermann, A., Danabasoglu, G., Deser, C., et al. (2021). Ubiquity of human-induced changes in climate variability. *Earth System Dynamics*, *12*(4), 1393–1411. https://doi.org/10.5194/esd-12-1393-2021

Tie, X., Brasseur, G., Emmons, L., Horowitz, L., & Kinnison, D. (2001). Effects of aerosols on tropospheric oxidants: A global model study. *Journal of Geophysical Research: Atmospheres*, *106*(D19), 22931–22964. https://doi.org/10.1029/2001JD900206

Tilmes, S., Mills, M. J., Zhu, Y., Bardeen, C. G., Vitt, F., Yu, P., et al. (2023). Description and performance of a sectional aerosol microphysical model in the Community Earth System Model (CESM2). *Geoscientific Model Development*, *16*(21), 6087–6125. https://doi.org/10.5194/gmd-16-6087-2023

Twomey, S. (1977). The Influence of Pollution on the Shortwave Albedo of Clouds. *Journal of the Atmospheric Sciences*, *34*(7), 1149–1152. https://doi.org/10.1175/1520-0469(1977)034%253C1149:TIOPOT%253E2.0.CO;2

Van Donkelaar, A., Martin, R. V., Leaitch, W. R., Macdonald, A. M., Walker, T. W., Streets, D. G., et al. (2008). Analysis of aircraft and satellite measurements from the Intercontinental Chemical Transport Experiment (INTEX-B) to quantify long-range transport of East Asian sulfur to

Canada. *Atmospheric Chemistry and Physics*, *8*(11), 2999–3014. https://doi.org/10.5194/acp-8-2999-2008

Yang, Y., Smith, S. J., Wang, H., Lou, S., & Rasch, P. J. (2019). Impact of Anthropogenic Emission Injection Height Uncertainty on Global Sulfur Dioxide and Aerosol Distribution. *Journal of Geophysical Research: Atmospheres*, *124*(8), 4812–4826. https://doi.org/10.1029/2018JD030001